Experimental and computational examination of anastellin (FnIII1c)-polymer interactions

David Mallinson[1], David L. Cheung[2*], Dorin Simionesie[3], Alexander B. Mullen[1], Zhenyu J. Zhang[3*], Dimitrios A. Lamprou[1,4,5*]

[1]Strathclyde Institute of Pharmacy and Biomedical Sciences (SIPBS), University of Strathclyde, 161 Cathedral Street, Glasgow, United Kingdom.

[2]School of Chemistry, National University of Ireland, Galway, University Road, Galway, Ireland.

[3]School of Chemical Engineering, University of Birmingham, Edgbaston, Birmingham, United Kingdom.

[4]Centre for Innovative Manufacturing in Continuous Manufacturing and Crystallisation (CMAC), University of Strathclyde, Glasgow, United Kingdom.

[5]New Address: Medway School of Pharmacy, University of Kent, Chatham, Kent, United Kingdom.

*Corresponding Authors. E-mails: david.cheung@nuigalway.ie, z.j.zhang@bham.ac.uk, d.lamprou@kent.ac.uk, Tel.: +44(0)1634202947

Keywords: Atomic force microscopy, molecular dynamics, polyurethane, poly (methyl methacrylate), fibronectin.

Abstract: Using a combination of experimental and computational approaches, the interaction between anastellin, a recombinant fragment of fibronectin, and representative biomaterial surfaces has been examined. Anastellin and superfibronectin, have been seen to exhibit anti-angiogenic properties and other properties that may make it suitable for consideration for incorporation into biomaterials. The molecular interaction was directly quantified by atomic force microscope (AFM) based force spectroscopy, complemented by adsorption measurements using quartz crystal microbalance (QCM). By AFM, it was found that the anastellin molecule facilitates a stronger adhesion on polyurethane films (72.0 pN nm^{-1}) than on poly (methyl methacrylate) films (68.6 pN nm^{-1}). However, this is not consistent with the QCM adsorption measurements which shows no significant difference. Molecular dynamics simulations of the behaviour of anastellin on polyurethane in aqueous solution were performed to rationalise the experimental data, and show that anastellin is capable of rapid adsorption to PU while its secondary structure is stable upon adsorption in water.

INTRODUCTION

In order to design medical devices that are exposed to physiological environments with prolonged service life and enhanced biocompatibility, it is vital to understand how biological objects interact with the surface of the engineered component, and the underlying biophysical mechanisms. For the development of biomaterials, the predominant mechanisms include the adsorption of proteins which is the initial stage for cell adhesion. [1] One of the major proteins that significantly affects the compatibility of biomaterials used intracorporeally is fibronectin (Fn). Fn is an important extracellular protein that exists in a variety of forms i.e. circulating plasma, tissue and cellular. [2] It is made up of three types of domain (I, II and III). Types I and

II are stabilised with disulphide bonds while type III Fn domains (FnIII) are capable of unfolding under tension. This can expose hidden, cryptic binding sites such as the Arg-Gly-Asp (RGD) sequence found in the tenth fibronectin type III domain (FnIII10) and the Pro-His-Ser-Arg-Asn (PHSRN) sequence in the ninth fibronectin type III domain (FnIII9). The RGD sequence allows binding to cell-bound integrin receptors, such as α5β1, to enable adhesion of cells to the extracellular matrix while the PHSRN sequence has a synergistic effect on this binding. [3] The RGD peptide sequence has been incorporated onto biomaterials, [4-6] in its linear form, or cyclic forms, or as part of a larger fragment in order to improve aspects of biocompatibility such as osseointegration. [4] Use of a protein fragment offers advantages over whole Fn such as improved stability and increased density of desired sequences on the surface. [7]

Another area of Fn that has been shown to elicit potentially useful interactions is the C-terminal fragment of the first FnIII domain (FnIII1c), known as anastellin, which has 76 amino acid residues. [8-12] The FnIII1 domain has been identified as a region associated with matrix formation by Fn-Fn interactions. [8] When mixed with whole Fn molecules, anastellin can create a different form of Fn known as superfibronectin which is adept at supporting cell adhesion and spreading. [10,13] Anastellin and superfibronectin have been reported to contribute towards anti-tumour, anti-metastatic, and anti-angiogenic performance through a mechanism that involves extracellular signal-regulated kinases (ERK) and a decrease in cyclin D1, cyclin Al, and cyclin-dependent kinase 4 (cdk4). [9,14-17]

Upon adsorption to solid surfaces, the conformation of Fn at the interface appears to depend largely on the characteristics of the surface. Fn has been seen to adopt an extended conformations on hydrophilic surfaces and compact, globular conformations on hydrophobic surfaces [18,19] Furthermore, other factors such as surface chemistry and topography have been found to play an important role. [20,21] Hydrophobic surfaces adsorb more Fn than hydrophilic

surfaces; [18] the globular conformation adopted by the protein means the surfaces could accommodate more molecules and hence exhibit a greater packing density. [22] The change of conformation to an elongated form is important since it can expose the aforementioned binding sites such as RGD and PHSRN and allow matrix formation and cell attachment. Interaction between protein and solid surface and the consequent confirmation can be examined with a wide range of experimental approaches including atomic force microscopy (AFM), quartz crystal microbalance, fluorescence resonance energy transfer (FRET), measuring the adsorption amount of labelled Fn, and enzyme-linked immunosorbent assays (ELISA). [18,19,23,24]

With the readily controlled molecular structure, chain length, and functional groups, polymers have been widely used as biomaterials. Examples include polyurethane (PU) for ureteral catheters, [25] poly (methyl methacrylate) (PMMA) for bone cement, [26] polytetrafluoroethylene (PTFE) for artificial heart valves and vascular grafts, [27] and ultra-high density polyethylene in joint replacement implants. Palacio *et al.* [28,29] have investigated the adhesion of whole Fn, bovine serum albumin and collagen to PMMA surfaces as well as di- and triblock copolymers of PMMA with poly (2-hydroxyethyl methacrylate) (PHEMA) and/or poly (acrylic acid) (PAA). They used AFM in force-volume mode with probes coated with silane and protein, and reported that the PMMA regions of the polymer had lower adhesion than PAA regions due to weaker interactions between the polymer and hydrophobic regions of Fn. The adhesive force between Fn and PMMA was reduced from 1.0 nN to 0.7 nN as the pH of the surrounding medium was decreased from 7.4 to 6.2. It is possible that the protein is less negatively charged at lower pH so that the electrostatic repulsion from the acid groups of the polymer is reduced.

For a number of years, a molecular simulation approach has been used to investigate protein-surface adsorption, [30] giving significant insight into the mechanism of adsorption and the

factors that drive this. Due to its relevance to biomaterials [1] the adsorption of a number of Fn modules onto surfaces have been investigated. [31-33] These have shown that Fn adsorption is relatively non-specific, with it readily adsorbing onto organic, [32] inorganic, [33] and graphite surfaces. [31]

In comparison with experimental methods molecular simulation can give significant insight into the early stages of protein adsorption and on the detailed microscopic information on the protein-surface interactions. Due to limitations on computer power, molecular dynamics are typically restricted to timescales of the order to 100 ns, so can only typically probe the initial stages of adsorption. These timescales are also typically unable to investigate large scale changes in protein structure, although techniques such as parallel tempering or metadynamics may be used to overcome this. Molecular dynamics simulations also depend on the accuracy of the simulation model; previous work [34] has suggested that of commonly used force fields the Charmm force field used in this work is most accurate.

MATERIALS AND METHODS

Materials

Poly (methyl methacrylate) (PMMA; 94,600 g mol^{-1}) was purchased from Acros Organics, New Jersey, USA. Polyurethane (PU; Selectophore^{TM}) and phosphate buffered saline (PBS; pH 7.4) tablets and diiodomethane (DIM; 99 %). were purchased from Sigma Aldrich, MO, USA. The FnIII1c protein fragment was purchased from Sigma Aldrich, Israel. Tetrahydrofuran (THF; ≥ 99.9 %) was from Sigma Aldrich, Germany. (3-aminopropyl)triethoxysilane (APTES; 99 %) was from Sigma Aldrich, China. Ethylene glycol (EG; 99.8 %) and ethanol (≥ 99.8 %) was purchased from Sigma Aldrich, United Kingdom.

Spin Coating

Silica wafer (SW; commercial available) was cleaned with deionised water (DW), followed by 70 % ethanol and finally with THF in order to sterilise the surface and remove both water-soluble and organic contaminants. Polymers were dissolved in THF (2 % w/v). Consequently, the polymer solution was spin coated onto SW at 2,000 rpm for 30 s with a Laurell WS-400-6NPP spin coater as per Mallinson *et al.* [35]

Contact Angle Goniometry

The advancing contact angles (θ_A) of three solvents (DW, EG and DIM) on the two polymer surfaces were measured in order to calculate the surface energy (γ_s) and surface energy components of the surfaces. As per Mallinson *et al.*, [35] small drops of DW (18.2 MΩ; surface tension (γ_L) 72.8 mN m^{-1} at 20 °C), EG (γ_L 48.0 mN m^{-1} at 20 °C) and DIM (γ_L 50.8 mN m^{-1} at 20 °C) were placed on the surface with a needle, followed by measuring both the left and right contact angles with a Krüss DSA30B contact angle goniometer (CAG). At least 2 repeats were made for each surface with 3 drops per sample, resulting in at least 12 measurements per sample. Using these contact angle values, the surface energies were calculated using a Visual Basic application developed by Lamprou *et al.*, [36] based on the formula proposed by Good and Oss. [37]

$$\gamma_s = \gamma_s^{LW} + \gamma_s^{AB} = \gamma_s^{LW} + 2\left(\gamma_s^+ \gamma_s^-\right)^{1/2} \quad \text{(Eq. 1a)}$$

$$\gamma_l = \gamma_l^{LW} + \gamma_l^{AB} = \gamma_l^{LW} + 2\left(\gamma_l^+ \gamma_l^-\right)^{1/2} \quad \text{(Eq. 1b)}$$

$$\gamma_l\left(1+\cos\theta\right) = 2\left[\left(\gamma_s^{LW}\gamma_l^{LW}\right)^{1/2} + \left(\gamma_s^+\gamma_l^-\right)^{1/2} + \left(\gamma_s^-\gamma_l^+\right)^{1/2}\right] \quad \text{(Eq. 2)}$$

where superscripts denote components of surface energy: Lifshitz-van der Waals *LW*, acid-base *AB*, Lewis acid γ^+ and Lewis base γ^-.

Atomic force microscopy

AFM measurements were performed in ambient using a Bruker Multimode 8 AFM equipped with a Nanoscope Controller V and SNL-10 probes (cantilever C: nominal spring constant 0.24 N m^{-1} and nominal resonant frequency 56 kHz). Cantilevers were silanised to allow protein functionalisation by submerging in 2 mM APTES in toluene for 5 min as per Couston *et al*. [38] The cantilevers were subsequently washed with toluene and DW in order to remove unbound silane. The FnIII1c protein fragment was added by incubating the tip in a drop of 1 mg mL^{-1} protein solution (in PBS pH 7.4) for 10 min followed by a thorough rinsing with deionised water to remove unbound protein. Each polymer surface was scanned in force-volume mode, which takes performs force curves in a grid, 4 times with each AFM probe before and after protein functionalisation. This was done with two different probes. For each of the AFM images approximately 160 curves were chosen at random from each of the force-volume images (20 curves x 4 areas x 2 probes). Deflection sensitivity was calibrated with a sapphire reference sample and the tip radius was determined with a PA01 spiked reference sample (Mikromasch). Ramps were made over 1 × 1 μm squares.

Surface roughness was determined using images captured using unfunctionalised probes in PeakForce-Quantitative Nanomechanical (PF-QNM) mode. Images were analysed with Bruker Nanoscope Analysis version 1.5 to view force curves and calculate surface roughness. Adhesion values were extracted from the ramps using an in-house Python script. Adhesive forces were then normalised for the effect of tip radius by dividing by tip radius in accordance with equation 3 by Sugawara *et al*. [39]

$$A = 4\pi RT \qquad \text{(Eq. 3)}$$

where A is the corrected adhesion, R is tip radius and T is surface tension of the medium.

Quartz Crystal Microbalance

Quartz crystal microbalance (QCM) is a technique that uses a mass sensor [40-42] to measure the adsorption of biopolymers [43,44] or synthetic electrolytes [45] from liquid and allows observation of not only the adsorption kinetics and adsorbed mass but also of the viscoelastic properties of adsorbed polymer layers at the solid liquid interface. [22,46,47] The technique relies upon the resonant frequency of a quartz crystal. A frequency shift (Δf) will be induced by any change in adsorbed mass, as Δf is related to the adsorbed mass per unit surface Δm, by a linear relationship known as the Sauerbrey equation (Eq. 4).

$$\Delta m = \frac{C\,\Delta f}{n} \qquad \text{(Eq. 4)}$$

where n is the overtone number (n = 1 in the present case) and C is a constant that describes the sensitivity of the device the changes in mass. Additionally, the exponential decay of the oscillation amplitude, D, is recorded which can reveal information about the viscoelastic properties of the adsorbed layer.

PU and PMMA thin films were formed on gold coated AT-cut quartz crystals by spin-coating, by the same protocol as on the SiO_2 wafers, and a SiO_2 crystal was used to replicate the SW surface. All crystals were purchased from Testbourne Ltd (United Kingdom). The crystals were placed in a home-built quartz crystal microbalance and all measurements were taken at room temperature. For adsorption measurements, the QCM chamber was flooded with HPLC-grade water and left until the frequency stabilises to an equilibrium state at the liquid/solid interface may be achieved. The protein fragment was initially dissolved in PBS buffer (pH 7.4) with a concentration of 1.0 mg mL^{-1}, and further diluted by HPLC-grade water to a concentration of 0.025 mg mL^{-1}. The HPLC-water in the QCM chamber was then replaced by the protein solution while the change in frequency and dissipation was recorded.

A representative QCM adsorption result is presented in Fig. 1 where changes in frequency and corresponding adsorbed amount are shown.

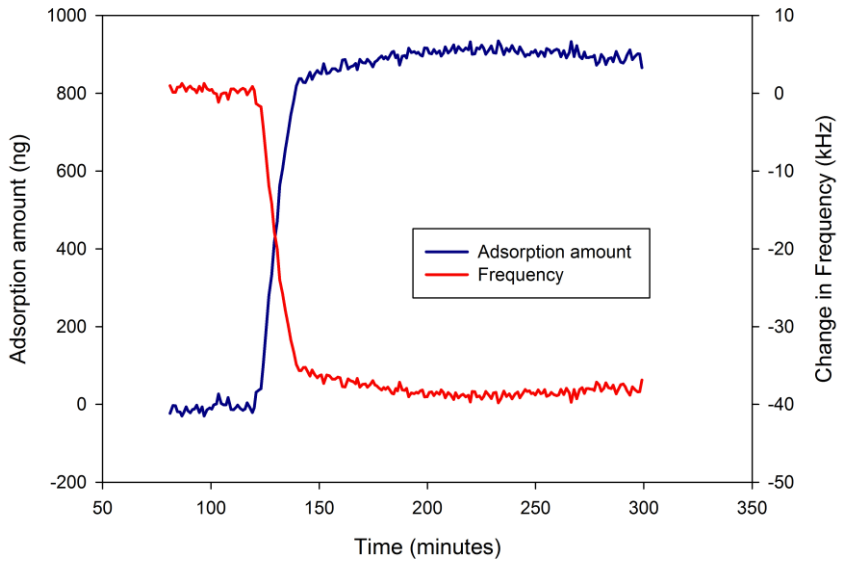

Fig. 1 Example of graph from QCM absorption measurements for anastellin showing changes in frequency and corresponding adsorbed amount.

Molecular dynamics

The simulated system consisted of a single anastellin molecule, a slab of PU, water and ions. To accurately model the protein adsorption a good description of polymer surfaces is necessary. The polymer surface was constructed using the crystal structure for the *trans*-*trans*-dicyclohexylmethane 4,4'-diisocynate (HMDI) monomer determined by Nigar *et al.* [48] To create a polymer chain this was duplicated and the PU surface was constructed from slab of crystalline PU, consisting of 48 chains (three layers of sixteen). An energy minimisation followed by short (20 ps) NVT and NpT simulations of the slab in contact with a vacuum were performed. The remainder of the simulation box was filled with water and an energy minimization and short NVT run were performed on the resulting system. The structure of the surface was then held fixed for the remainder of the simulations.

The structure of anastellin was taken from RCSB (accession code: 1Q38). Initially the protein centre-of-mass is placed at z = 40 Å, approximately 20 Å from the PU surface. Four different initial orientations were used: Arg-down where the cluster of arginine residues was orientated towards the surface; Arg-up where the cluster of arginine residues orientated away from the surface; N-down where the N-terminus pointed towards the surface and C-down where the C-terminus pointed towards the surface. Cl^- and Na^+ ions are added to neutralise the +5e charge on the protein and simulate different salt conditions. The system is periodic in the *x* and *y* directions and has repulsive Lennard-Jones walls in the *z*-direction.

The protein was modelled using the Charmm27 force field (with CMAP corrections), [49] the Charmm Generalised Force Field [50] was used to model the PU surface, and water was modelled using the Charmm-variant of TIP3P water (with van der Waals interaction sites on the hydrogen atoms). All simulations were performed at 298 K, with the velocity rescaling algorithm of Bussi *et al*. [51] used to control the temperature. For each starting orientation and salt concentration simulations of 100 ns were performed, with a timestep of 2 fs. Bonds involving hydrogen atoms were constrained using the LINCS algorithm [52] and the water geometry was held fixed using the SETTLE algorithm. [53] Long-range electrostatics were modelled using particle-mesh Ewald summation [54] with a real space cut-off of 10 Å and a reciprocal space grid spacing of 0.16 $Å^{-1}$. Van der Waals interactions were truncated at 10 Å.

The simulations were performed using the Gromacs MD package, version 4.6.3. [55] Standard Gromacs tools were used to set up and analyse the simulations.

Statistical Analysis

Statistical analysis was performed in Microsoft Excel, Python and Minitab 17. A significance level of 5 % was chosen. Significance between adhesive forces under different conditions were determined with a one-way ANOVA with a Tukey test.

RESULTS AND DISCUSSION

Contact Angle Goniometry and Surface Energies

The contact angles of water on all substrates used are presented in Table 1 and agree well with the literature values for PMMA (74 ° [56] and 69 ° [28]), PU (85.1 ° [35]) and silica wafer (57.9 ° [35]). From the chemical structures of PU and PMMA, it can be estimated that PMMA would be more hydrophobic since displays a greater frequency of lone electron pairs. The surface energies and surface energy components for all the surfaces are shown in Table 2. The R_a values (Table 2), based on the surface topography images collected with AFM, show that the films are smooth – 2.0 ± 0.1 nm and 3.1 ± 0.3 nm R_a for PMMA and PU respectively. This suggests that the adsorption of Fn [57] and water contact angle [35] are not affected by surface roughness.

Table 1 Advancing contact angles of SW, PMMA and PU surfaces, n = 12.

Table 2 Surface energy components by CAG and surface roughness by AFM of SW, PMMA, and PU surfaces.

Atomic Force Microscopy

Anastellin functionalisation increases adhesion on all surfaces tested (Fig. 2). The differences between the PMMA (16.8 % increase) and PU (12.5 % increase) values are greater than those between the silica values (48.2 % increase). Since tip radius is accounted for, the difference between the polymers and the APTES-functionalised and protein-ATPES-functionalised probes is likely due to hydrophilic-hydrophobic interactions between protein fragment and elements of the polymer chains as found by Palacio *et al*. with the interactions between Fn

and PMMA and PAA. [28] It appears that the adhesion of the anastellin-functionalised probes to the PU films was greater than to PMMA films (data not shown), contrary to previous work. This could be at least partly due to the fact that while Palacio *et al*.'s [28] experiments were performed under liquid these were performed in air at ambient humidity reducing the role of hydrophilic-hydrophobic interactions.

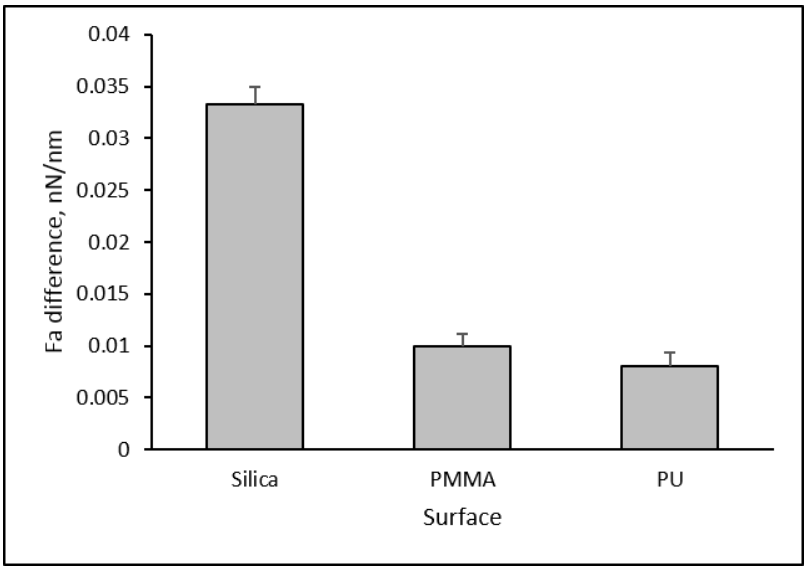

Fig. 2 Difference in adhesion force by surface between silanised probes (APTES) and protein-functionalised probes (anastellin). All differences are significant.

Quartz crystal microbalance

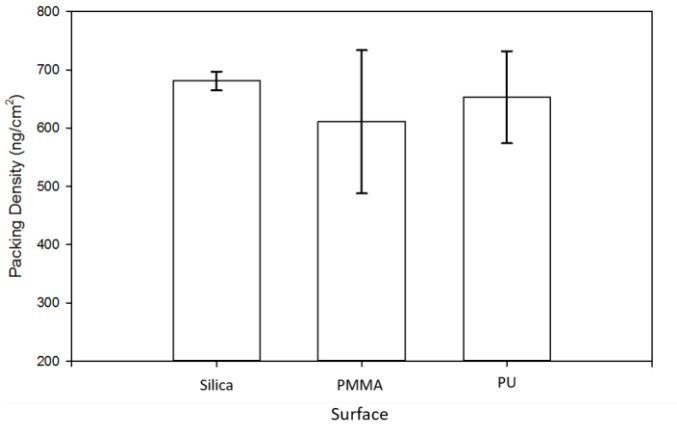

Fig. 3 Density of anastellin on SiO_2, PU and PMMA surfaces.

Fig. 1 shows a representative measurement of protein adsorption on PMMA, in which both frequency and the corresponding mass change are presented as a function of time. It is clear that upon the introduction of protein solution, the mass at the already equilibrated polymer-buffer solution interface is increased, which confirms the adsorption of protein on the polymeric film. The adsorption amounts of the protein (the changed frequency) on three different surfaces are compared in Fig. 3. It was found that protein adsorbed the most on the silica surface, which is consistent with the AFM measurements where strong adhesion between protein and silica surface was observed. The PU surface shows a higher adsorption than the PMMA despite the large error bar. The increase in experimental error between silica and the polymer coated surfaces could be due to the increased surface roughness on the polymer thin films.

Molecular dynamics

The adsorption mechanism and adhesion of anastellin to the polymer surfaces required further investigation by molecular dynamics. Due to the high adsorption in the QCM studies, PU was selected for these further studies.

Independent of starting orientation the protein adsorbs onto PU surface within 100 ns, however, the protein-surface separation and orientation at the end of the simulation depend on the initial configuration (Fig. 4). Starting from the Arg-down configuration the protein adsorbs rapidly onto the surface with little change in the orientation (the protein lies parallel to the surface across the entire simulation). In this case the final protein centre of mass position is ~32 Å, which is comparable to the width of the PU layer plus half the protein width. For the other starting configurations, adsorption typically takes longer and often involves transient contacts between the surface and protein before permanent adsorption. Additionally, the final separation between the protein centre-of-mass and surface is substantially larger, suggesting that in these cases the bulk of the protein lies further from the surface. This can be seen through the protein orientation. In particular, when starting from the Arg-up configuration the protein reorients so the N-terminus is towards the surface, so the final orientation of the protein in this case is close to that found form starting in the N-down conformation. For the C-down starting conformation, for most of the simulation the protein lies normal to the surface with the C-terminus pointing down (θ ~180 °) but slow reorientations of the protein are evident, notably towards the end of the simulation.

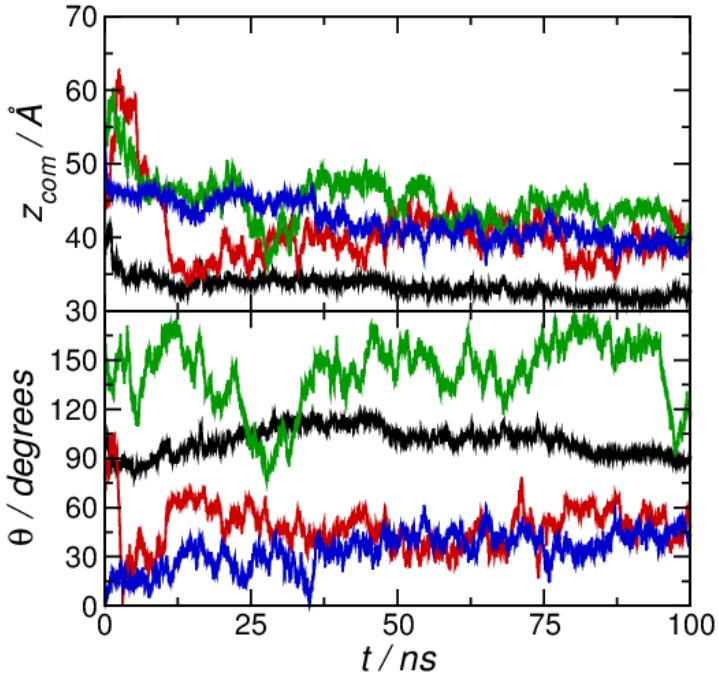

Fig. 4 Protein centre-of-mass position (top) and orientation (bottom) for no salt simulations. Simulations starting in the Arg-down, Arg-up, C-down, and N-down conformations are denoted by black, red, green, and blue lines respectively.

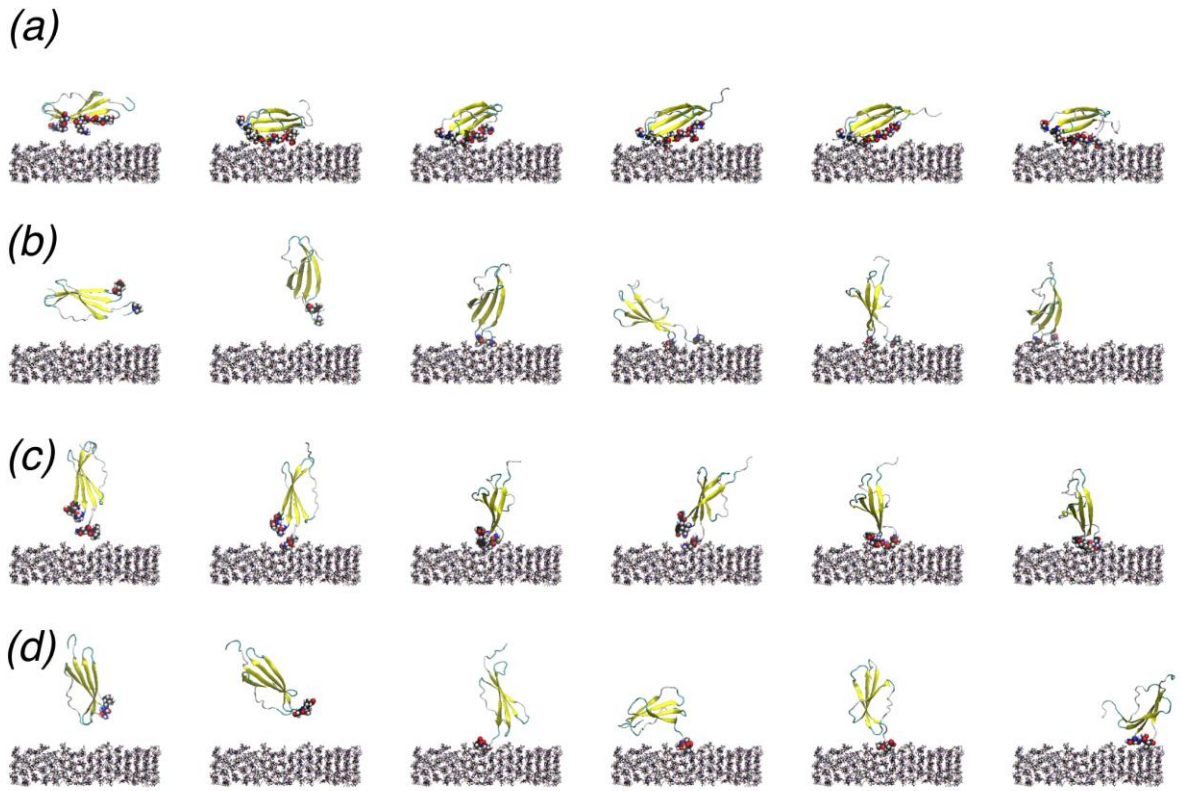

Fig. 5 Simulation snapshots showing adsorption of anastellin on to polyurethane surface. (a) Protein in Arg-down starting configuration at (left to right) t = 0, 13, 25, 47, 50, and 100 ns. (b) Protein in Arg-up starting configuration at (left to right) t = 0, 5, 10, 48, 55, and 100 ns. (c) Protein in N-down starting configuration at (left to right) t = 0, 1, 15, 20, 50, and 100 ns.

(d) Protein in C-down starting configuration at (left to right) t = 0, 1, 10, 27.5, 47, and 100 ns. Residues involved in adsorption (see text) are highlighted.

Qualitative information on protein adsorption may be found from viewing simulation snapshots. For the Arg-down conformation (Fig. 5), these show the rapid adsorption of the protein onto the PU surface, with little subsequent change to either the protein structure or orientation. From the Arg-up conformation, the protein initially reorients itself in solution so that the N-terminus is directed towards the surface (t = 5 ns), followed by attachment to the surface through this region. While adsorbed on the surface, the protein can slowly reorient. Similarly, when the protein is initially placed in the N-down conformation, the protein's N-terminus rapidly adsorbs onto the surface (t = 1 ns). For the C-down conformation the protein attaches through the C-terminus (t = 10 ns) but more slowly than for N-down conformation (whereas the N-down conformation attached to the surface after only 1 ns the C-down conformation is still in bulk water at this time). Compared to the N-down conformation the protein appears to have greater orientational freedom, which may also be seen from the variation in protein angle over time. While the initial attachment is through the residues at the extreme end of the C-terminus, this changes towards the end of the simulation, with residues at the C-terminus end of the beta-sheet coming into contact with the surface.

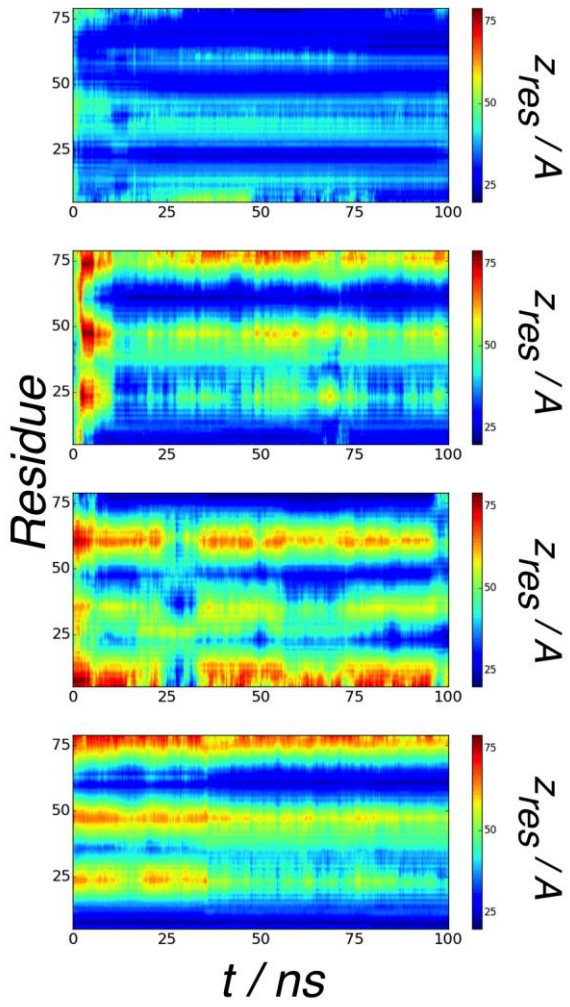

Fig. 6 Residue centre-of-mass positions for protein starting in (top to bottom) Arg-down, Arg-up, C-down, and N-down conformations.

The different starting orientations lead to attachment through different regions of the protein. This may be seen through considering the centre-of-mass positions of the individual residues (Fig. 6). Apart from the Arg-down conformation, in which most of the residues lie close to the surface, only small numbers of residues are typically in contact with the surface. For both Arg-up and N-down these are the N-terminus and the loop joining the third and fourth beta-strands (around residue 61). This second region contains a number of residues with hydrophilic side-chains, which are capable of forming hydrogen bonds with the polar groups in the PU surface. For the C-down orientation while the initial contact is through the C-terminal end at the end of the simulation this has detached from the surface with a loop

containing residues 22 to 26 (joining the first and second beta-strands). Again this is a predominately hydrophilic region, which is consistent with the highest adsorption being found for hydrophilic surfaces. The residues that are in contact with the surface (taken to be those with separation between the surface and centres-of-mass less than 5 Å) are shown in Table 3.

Table 3 Residues in contact with surface

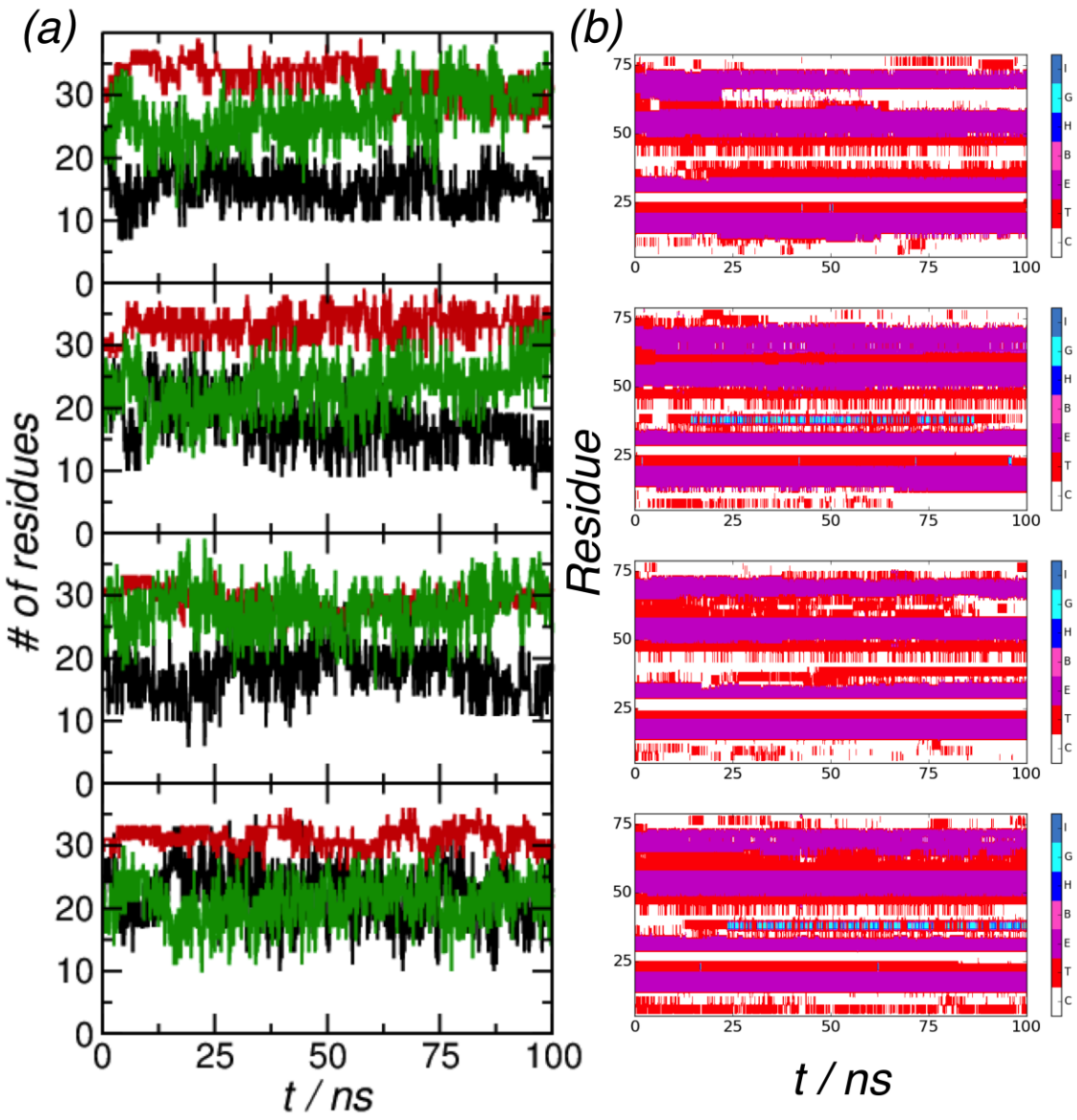

Fig. 7 (a) Secondary structure amounts for (top to bottom) Arg-down, Arg-up, C-down, and N-down starting conformations. Black, red, and green lines denote turn, beta-strand, and random coil respectively. (b) Secondary structure distributions for (top to bottom) Arg-down, Arg-up, C-down, and N-down starting conformations. (C random coil, T turn, E extended, B bridge, H alpha-helix, G 3/10-helix, and I pi-helix).

The initial stages of surface adsorption have little effect on the structure of the protein. Shown in Fig. 7a are the secondary structure compositions for the different starting structures. In all cases the structure remains predominately beta-strand, with turn and random coil. Apart from N-down, there is a slight increase in the amount of random coil when the

protein adsorbs, with the amount of turn decreasing. The distribution of the different secondary structure motifs is also largely unchanged during the simulations (Fig. 7b). It should be noted this only applies to the initial stages of adsorption significant changes in protein structure may occur over longer timescales.

From consideration of all of the simulations it may be seen that three particular regions of the protein are especially important in mediating attachment; these are the loop joining the first and second beta-strands (around residue 23), the loop joining the third and fourth beta-strands, and the C-terminus. These contain predominately hydrophilic residues, with attachment being driven by hydrogen bonding between these groups and the N-H and C=O groups in the PU. Adsorption through flexible regions suggests that these play a role in mediating surface adsorption, similar to the fly-casting mechanism exhibited by some DNA-binding proteins. [58]

The use of silanisation to functionalise the AFM probe means that the protein attaches to the probe via the N-terminal [59] since this allows covalent bonding. Protein that is not covalently bonded to the AFM probe ought to be removed by the washing stages. This method for protein functionalisation has been used previously for antibodies [38] and for Fn. Attachment of protein by the N-terminal would suggest that the C-down, Arg-down and Arg-up orientations used in the MD simulations are most relevant to the situation in the AFM experiments while all orientations are relevant to the QCM experiments.

CONCLUSION

In this paper the adsorption of anastellin, a C-terminal fragment of the fibronectin type III domain, onto biomaterial surfaces was investigated using a combination of experimental and theoretical methods. Understanding the adsorption of proteins onto synthetic surfaces is of

interest in the development of new materials for medical applications. Anastellin may have a role in biomaterials for its role in the formation of superfibronectin; and its anti-tumorigenic and anti-angiogenic properties. By combining a number of different methods, this work provides a picture of the adsorption ranging from the molecular to macroscopic levels.

Agreement between adhesion data and adsorption results confirm that there is greater interaction between anastellin and PU than between anastellin and PMMA. Molecular dynamics simulations of anastellin on polyurethane show that adsorption occurs irrespective of the starting orientation of the protein, suggesting that this is relatively non-specific. Analysis of the simulations suggest that adsorption onto polyurethane is mediated by hydrophilic amino acids, due to hydrogen bonding with C=O and N-H groups in the polymer backbone, and residues in flexible regions of the protein.

ACKNOWLEDGMENTS

The authors would like to acknowledge the UK Engineering & Physical Sciences Research Council (EPSRC) and the University of Strathclyde for the studentship to David Mallinson, and the Bridging the gap (BTG) project at the University of Strathclyde for funding this work. Computational facilities were provided by the Archie-West HPC facility (EPSRC grant no. EP/K000586/1), and SFI/HEA Irish Centre for High-End Computing (ICHEC) and access to AFM and contact angle measurements was provided by the EPSRC Centre in Continuous Manufacturing and Crystallisation (CMAC).

References

1. Vanterpool FA, Cantini M, Seib FP, Salmeron-Sanchez M. A material-based platform to modulate fibronectin activity and focal adhesion assembly. Biores Open Access 2014;3(6):286-96.
2. To WS, Midwood KS. Plasma and cellular fibronectin: distinct and independent functions during tissue repair. Fibrogenesis & Tissue Repair 2011;4(1):1-17.
3. Aota S, Nomizu M, Yamada KM. The short amino-acid-sequence Pro-His-Ser-Arg-Asn in human fibronectin enhances cell-adhesive function. Journal of Biological Chemistry 1994;269(40):24756-24761.
4. Agarwal R, González-García C, Torstrick B, Guldberg RE, Salmerón-Sánchez M, García AJ. Simple coating with fibronectin fragment enhances stainless steel screw osseointegration in healthy and osteoporotic rats. Biomaterials 2015;63:137-145.
5. Herranz-Diez C, Mas-Moruno C, Neubauer S, Kessler H, Gil FJ, Pegueroles M, Manero JM, Guillem-Marti J. Tuning Mesenchymal Stem Cell Response onto Titanium-Niobium-Hafnium Alloy by Recombinant Fibronectin Fragments. ACS Appl Mater Interfaces 2016;8(4):2517-25.
6. Petrie TA, Capadona JR, Reyes CD, Garcia AJ. Integrin specificity and enhanced cellular activities associated with surfaces presenting a recombinant fibronectin fragment compared to RGD supports. Biomaterials 2006;27(31):5459-70.
7. Hersel U, Dahmen C, Kessler H. RGD modified polymers: biomaterials for stimulated cell adhesion and beyond. Biomaterials 2003;24(24):4385-4415.
8. Morla A, Ruoslahti E. A fibronectin self-assembly site involved in fibronectin matrix assembly: reconstruction in a synthetic peptide. J Cell Biol 1992;118(2):421-9.
9. Yi M, Ruoslahti E. A fibronectin fragment inhibits tumor growth, angiogenesis, and metastasis. PNAS 2001;98(2):620-4.
10. Morla A, Zhang Z, Ruoslahti E. Superfibronectin is a functionally distinct form of fibronectin. Nature 1994;367:193-6.
11. Kelsh R, You R, Horzempa C, Zheng M, McKeown-Longo PJ. Regulation of the innate immune response by fibronectin: synergism between the III-1 and EDA domains. PLoS One 2014;9(7):e102974.
12. Stine JM, Sun Y, Armstrong G, Bowler BE, Briknarova K. Structure and unfolding of the third type III domain from human fibronectin. Biochemistry 2015;54(44):6724-33.
13. Ohashi T, Erickson H. Domain unfolding plays a role in superfibronectin formation. J Biol Chem 2005;280(47):39143-51.
14. Zheng M, Jones DM, Horzempa C, Prasad A, McKeown-Longo PJ. The First Type III Domain of Fibronectin is Associated with the Expression of Cytokines within the Lung Tumor Microenvironment. J Cancer 2011;2:478-83.
15. Ambesi A, Klein M, Pumiglia K, McKeown-Longo P. Anastellin, a fragment of the first type III repeat of fibronectin, inhibits extracellular signal-regulated kinase and causes G1 arrest in human microvessel endothelial cells. Cancer Res 2005;65:148-56.
16. Ambesi A, McKeown-Longo PJ. Anastellin, the angiostatic fibronectin peptide, is a selective inhibitor of lysophospholipid signaling. Mol Cancer Res 2009;7(2):255-65.
17. You R, Zheng M, McKeown-Longo PJ. The first type III repeat in fibronectin activates an inflammatory pathway in dermal fibroblasts. J Biol Chem 2010;285(47):36255-9.
18. Kowalczynska H, Nowak-Wyrzykowska M, Kolos R, Dobkowski J, Kaminski J. Fibronectin adsorption and arrangement on copolymer surfaces and their significance in cell adhesion. J Biomed Mater Res Part A 2005;72A(2):228-36.

19. Baugh L, Vogel V. Structural changes of fibronectin adsorbed to model surfaces probed by fluorescence resonance energy transfer. J Biomed Mater Res Part A 2004;69A(3):525-34.
20. Michael K, Vernekar V, Keselowsky B, Meredith J, Latour R, Garcia A. Adsorption-induced conformational changes in fibronectin due to interactions with well-defined surface chemistries. Langmuir 2003;19(19):8033-40.
21. Thevenot P, Hu W, Tang L. Surface chemistry influences implant biocompatibility. Curr Top Med Chem 2008;8(4):270-80.
22. Roach P, Farrar D, Perry CC. Interpretation of protein adsorption: Surface-induced conformational changes. J Am Chem Soc 2005;127(22):8168-8173.
23. Krammer A, Lu H, Isralewitz B, Schulten K, Vogel V. Forced unfolding of the fibronectin type III module reveals a tensile molecular recognition switch. PNAS 1999;96(4):1351-1356.
24. Kowalczynska HM, Kolos R, Nowak-Wyrzykowska M, Dobkowski J, Elbaum D, Szczepankiewicz A, Kaminski J. Atomic force microscopy evidence for conformational changes of fibronectin adsorbed on unmodified and sulfonated polystyrene surfaces. J Biomed Mater Res Part A 2009;91A(4):1239-1251.
25. Lange D, Chew BH. Update on ureteral stent technology. Ther Adv Urol 2009;1(3):143-8.
26. Webb JCJ, Spencer RF. The role of polymethylmethacrylate bone cement in modern orthopaedic surgery. J Bone Joint Surg 2007;89-B(7):851-857.
27. Cassady AI, Hidzir NM, Grøndahl L. Enhancing expanded poly(tetrafluoroethylene) (ePTFE) for biomaterials applications. J Appl Polym Sci 2014;131(15).
28. Palacio M, Schricker S, Bhushan B. Bioadhesion of various proteins on random, diblock and triblock copolymer surfaces and the effect of pH conditions. J R Soc Interface 2011;8(58):630-40.
29. Palacio M, Schricker S, Bhushan B. Protein conformation changes on block copolymer surfaces detected by antibody-functionalized atomic force microscope tips. J Biomed Mater Res Part A 2012;100A(1):18-25.
30. Szott LM, Horbett TA. Protein interactions with surfaces: cellular responses, complement activation, and newer methods. Curr Opin Chem Biol 2011;15(5):677-682.
31. Raffaini G, Ganazzoli F. Molecular dynamics simulation of the adsorption of a fibronectin module on a graphite surface. Langmuir 2004;20(8):3371-8.
32. Panos M, Sen TZ, Ahunbay MG. Molecular simulation of fibronectin adsorption onto polyurethane surfaces. Langmuir 2012;28(34):12619-12628.
33. Kubiak-Ossowska K, Mulheran P, Nowak W. Fibronectin module FNIII9 adsorption at contrasting model surfaces studied by atomistic molecular dynamics. J Phys Chem B 2014;118(33):9900-8.
34. Collier G, Vellore NA, Yancey JA, Stuart SJ, Latour RA. Comparison between empirical protein force fields for the simulation of the adsorption behavior of structured LK peptides on functionalized surfaces. Biointerphases 2012;7(1):24.
35. Mallinson D, Alexiou P, Mullen A, Pelecanou M, Sagnou M, Lamprou DA. Isatin thiosemicarbazone-blended polymer films for biomedical applications: surface morphology, characterisation and preliminary biological assessment. RSC Advances 2016.
36. Lamprou D, Smith J, Nevell T, Barbu E, Willis C, Tsibouklis J. Towards the determination of surface energy at the nanoscale: a further assessment of the AFM-based approach. J Adv Microscopy Res 2010;5:137-42.

37. Good R, van Oss C. The modern theory of contact angles and the hydrogen bond components of surface energies. In: G SMaL, editor. Modern Approach to Wettability: Theory and Applications. New York: Plenum; 1992.
38. Couston R, Lamprou D, Uddin S, van der Walle C. Interaction and destabilization of a monoclonal antibody and albumin to surfaces of varying functionality and hydrophobicity. Int J Pharm 2012;438:71-80.
39. Sugawara Y, Ohta M, Konishi T, Morita S, Suzuki M, Enomoto Y. Effects of humidity and tip radius on the adhesive force measured with atomic force microscopy. Wear 1993;168(1–2):13-16.
40. Rodahl M, Hook F, Kasemo B. QCM operation in liquids: An explanation of measured variations in frequency and Q factor with liquid conductivity. Anal Chem 1996;68(13):2219-2227.
41. Kanazawa KK, Gordon JG. The oscillation frequency of a quartz resonator in contact with a liquid. Anal Chim Acta 1985;175(SEP):99-105.
42. Schumacher R, Borges G, Kanazawa KK. The quartz microbalance - a sensitive tool to probe surface reconstructions on gold electrodes in liquid. Surf Sci 1985;163(1):L621-L626.
43. Hayakawa T, Yoshinari M, Nemoto K. Characterization and protein-adsorption behavior of deposited organic thin film onto titanium by plasma polymerization with hexamethyldisiloxane. Biomaterials 2004;25(1):119-127.
44. Hook F, Voros J, Rodahl M, Kurrat R, Boni P, Ramsden JJ, Textor M, Spencer ND, Tengvall P, Gold J and others. A comparative study of protein adsorption on titanium oxide surfaces using in situ ellipsometry, optical waveguide lightmode spectroscopy, and quartz crystal microbalance/dissipation. Colloids Surf B 2002;24(2):155-170.
45. Wagberg L, Pettersson G, Notley S. Adsorption of bilayers and multilayers of cationic and anionic co-polymers of acrylamide on silicon oxide. J Colloid Interface Sci 2004;274(2):480-488.
46. Tammelin T, Merta J, Johansson LS, Stenius P. Viscoelastic properties of cationic starch adsorbed on quartz studied by QCM-D. Langmuir 2004;20(25):10900-10909.
47. Wolff O, Seydel E, Johannsmann D. Viscoelastic properties of thin films studied with quartz crystal resonators. Farad Discuss 1997;107:91-104.
48. Nigar M, Blackwell J, Chvalun SN, Seneker SD, Schmelzer HG. The structure of the hard domains in trans,trans-HMDI-based polyurethane elastomers. Acta Polym 1996;47(1):48-54.
49. MacKerell AD, Bashford D, Bellott M, Dunbrack RL, Evanseck JD, Field MJ, Fischer S, Gao J, Guo H, Ha S and others. All-atom empirical potential for molecular modeling and dynamics studies of proteins. J Phys Chem B 1998;102(18):3586-616.
50. Vanommeslaeghe K, Hatcher E, Acharya C, Kundu S, Zhong S, Shim J, Darian E, Guvench O, Lopes P, Vorobyov I and others. CHARMM general force field: A force field for drug-like molecules compatible with the CHARMM all-atom additive biological force fields. J Comput Chem 2010;31(4):671-690.
51. Bussi G, Donadio D, Parrinello M. Canonical sampling through velocity rescaling. J Chem Phys 2007;126(1):014101.
52. Hess B. P-LINCS: A parallel linear constraint solver for molecular simulation. J Chem Theory Comput 2008;4(1):116-122.
53. Miyamoto S, Kollman PA. Settle: An analytical version of the SHAKE and RATTLE algorithm for rigid water models. J Comput Chem 1992;13(8):952-962.
54. Essmann U, Perera L, Berkowitz ML, Darden T, Lee H, Pedersen LG. A smooth particle mesh Ewald method. J Chem Phys 1995;103(19):8577-8593.

55. Hess B, Kutzner C, van der Spoel D, Lindahl E. GROMACS 4: Algorithms for highly efficient, load-balanced, and scalable molecular simulation. J Chem Theory Comput 2008;4(3):435-447.
56. Dann JR. Forces involved in the adhesive process. J Colloid Interface Sci 1970;32(2):321-331.
57. Elter P, Lange R, Beck U. Atomic force microscopy studies of the influence of convex and concave nanostructures on the adsorption of fibronectin. Colloids and surfaces B Biointerfaces 2012;89:139-46.
58. Levy Y, Onuchic JN, Wolynes PG. Fly-casting in protein-DNA binding: frustration between protein folding and electrostatics facilitates target recognition. J Am Chem Soc 2007;129(4):738-9.
59. Aissaoui N, Bergaoui L, Landoulsi J, Lambert J-F, Boujday S. Silane layers on silicon surfaces: mechanism of interaction, stability, and influence on protein adsorption. Langmuir 2012;28(1):656-665.

Figure captions

Fig. 1 Example of graph from QCM absorption measurements for anastellin showing changes in frequency and corresponding adsorbed amount.**Error! Reference source not found.**

Fig. 2 Difference in adhesion force by surface between silanised probes (APTES) and protein-functionalised probes (anastellin). All differences are significant.

Fig. 3 Density of anastellin on SiO2, PU and PMMA surfaces.

Fig. 4 Protein centre-of-mass position (top) and orientation (bottom) for no salt simulations. Simulations starting in the Arg-down, Arg-up, C-down, and N-down conformations are denoted by black, red, green, and blue lines respectively.

Fig. 5 Simulation snapshots showing adsorption of anastellin on to polyurethane surface. (a) Protein in Arg-down starting configuration at (left to right) t = 0, 13, 25, 47, 50, and 100 ns. (b) Protein in Arg-up starting configuration at (left to right) t = 0, 5, 10, 48, 55, and 100 ns. (c) Protein in N-down starting configuration at (left to right) t = 0, 1, 15, 20, 50, and 100 ns. (d) Protein in C-down starting configuration at (left to right) t = 0, 1, 10, 27.5, 47, and 100 ns. Residues involved in adsorption (see text) are highlighted..

Fig. 6 Residue centre-of-mass positions for protein starting in (top to bottom) Arg-down, Arg-up, C-down, and N-down conformations.

Fig. 7 (a) Secondary structure amounts for (top to bottom) Arg-down, Arg-up, C-down, and N-down starting conformations. Black, red, and green lines denote turn, beta-strand, and random coil respectively. (b) Secondary structure distributions for (top to bottom) Arg-down, Arg-up, C-down, and N-down starting conformations.**Error! Reference source not found.**

Table 1 Advancing contact angles of SW, PMMA and PU surfaces, n = 12.

	Contact Angle (θ_A °)		
Surface	DW	DIM	EG
SW	**56.6 ± 1.3**	**42.2 ± 2.6**	**33.9 ± 6.5**
PMMA	**74.7 ± 3.8**	**40.7 ± 1.1**	**59.2 ± 2.5**
PU	**85.9 ± 12.2**	**42.1 ± 7.5**	**60.0 ± 1.6**

Table 2 Surface energy components by CAG and surface roughness by AFM of SW, PMMA, and PU surfaces.

	Surface energy (mJ m^{-2})				Roughness by AFM
Surface	γ_s^{LW}	γ_s^+	γ_s^-	γ_s	Ra (nm)
SW	**38.49**	**0.30**	**23.98**	**43.81**	**0.11 ± 0.01**
PMMA	**39.26**	**0.14**	**13.63**	**42.02**	**2.00 ± 0.11**
PU	**38.54**	**0.00**	**4.07**	**38.67**	**3.06 ± 0.25**

Table 3 Residues in contact with surface

Conformation	Residues in Contact
Arg-down	K21, N23, Q64, E65, T67, R68, D70
Arg-up	P7, Y61
C-down	N21, V23
N-down	A6, P7, Q8, Q60, Y61, G62

Equations

Equation 1a

$$\gamma_s = \gamma_s^{LW} + \gamma_s^{AB} = \gamma_s^{LW} + 2\left(\gamma_s^+ \gamma_s^-\right)^{1/2}$$

Equation 1b

$$\gamma_l = \gamma_l^{LW} + \gamma_l^{AB} = \gamma_l^{LW} + 2\left(\gamma_l^+ \gamma_l^-\right)^{1/2}$$

Equation 2

$$\gamma_l\left(1+\cos\theta\right) = 2\left[\left(\gamma_s^{LW}\gamma_l^{LW}\right)^{1/2} + \left(\gamma_s^+\gamma_l^-\right)^{1/2} + \left(\gamma_s^-\gamma_l^+\right)^{1/2}\right]$$

Superscripts denote components of surface energy: Lifshitz-van der Waals *LW*, acid-base *AB*, Lewis acid γ^+ and Lewis base γ^-.

Equation 3

$A = 4\pi RT$

Equation 4 Sauerbrey equation

$$\Delta m = \frac{c\Delta f}{n}$$